Unlocking Enhanced Electrochemical Performance of MBene-MoB Through Controlled Aluminum Dissipation from MoAlB

Shudan Wei,* Girish Kale,* and Xiaojun Lai

2D transition metal borides, known as MBenes, have attracted considerable attention due to their exceptional properties. This study explores the feasibility of aluminum (Al) etching from MoAlB using environmentally friendly and sustainable fluoride-free dilute acidic/alkaline solutions at room temperature, revealing its thermodynamic and kinetic viability. Furthermore, it is found that complete removal of Al can be achieved in dilute alkaline reagent under hydrothermal conditions, yielding pristine single/few-layered MBene-MoB for the first time, while acidic solutions result in ≈33% etching rates. XRD refinement, which tracks aluminum removal from 0% to 100%, reveals transient metastable phases of $MoAl_{1-x}B$ ($x < 0.5$) in the initial etching stages, evolving into relatively stable pure Mo_2AlB_2 structures with 50% Al deficiency, serving as a precursor to MBenes. The subsequent loss of Al results in a 2D MBene-MoB structure. DFT calculations confirm excellent conductivity for MoAlB, $MoAl_{1-x}B$ ($x = 0$–1), and MBene-MoB. Remarkably, MBene-MoB exhibits superior supercapacitor performance with a 4025.60 mF cm^{-2}/201.28 F g^{-1} capacitance. Simulations validate rapid electrolyte diffusion in layered MBene-MoB, contributing significantly to enhanced capacitance. Additionally, in the hydrogen evolution reaction (HER), MBene-MoB demonstrates superior catalytic activity compared to the precursor MoAlB and commercial MoB. Calculations suggest the potential for enhancing HER through surface modulation, considering its suboptimal hydrogen adsorption energy.

1. Introduction

In the realm of advanced materials, the fascination with 2D materials stems from their exceptional properties, such as high surface area and superior conductivity.[1] MXenes, a prominent member of the 2D material family, has shown great promise in applications ranging from electrocatalysis to energy storage.[2] However, challenges persist, particularly in the harsh etching conditions required for MXenes synthesis, involving hydrofluoric acid (HF) and high-temperature concentrated etchants.[3] Moreover, the inherent surface oxidation of MXenes poses structural stability issues, limiting its long-term catalytic activity and stability in aqueous electrochemical applications.[4] A recent breakthrough in the field introduces MBenes, a novel class of 2D transition metal borides synthesized by selectively etching an intermediate aluminum layer from layered parent transition metal aluminium boride solids (MAB phases). These MBenes exhibit outstanding properties, including an ultra-high Young's modulus, exceptional electronic conductivity, and remarkable stability. Notably, they demonstrate exceptional resistance to corrosion and surface oxidation in aqueous media, making them highly promising for applications in electrochemical energy storage and catalysis.[1c,5]

While some MBenes have been explored in electrochemical energy storage and conversion, including lithium-sulfur batteries,[6] lithium batteries,[7] Na/K Ion Batteries,[8] partially dealuminated supercapacitors,[9] and hydrogen evolution,[10] oxygen evolution,[11] there remains a critical need to understand their environmental sustainable synthesis methods and etching mechanisms. Overcoming these challenges is vital for expanding their applications. The formidable obstacle lies in the strong metal–metal (M–A) and A—B bonds within the interlayers of MAB, making it challenging to achieve the selective etching required for the 2D delamination of MBenes monolayers.[12] Current etching methods, including fluoride etching, lack mildness and often result in impure MBenes materials and incompleted Al removal.[13] Some studies have explored molten salt-assisted high-temperature calcination for etching, achieving increased aluminum removal. However, the high temperature stabilizes impurity aluminum oxides, complicating their removal process.[14] Furthermore, a paucity of experimental studies exists

S. Wei, G. Kale, X. Lai
School of Chemical and Process Engineering
University of Leeds
Leeds LS2 9JT, UK
E-mail: pmswei@leeds.ac.uk; g.m.kale@leeds.ac.uk

ADVANCED
SCIENCE NEWS
www.advancedsciencenews.com

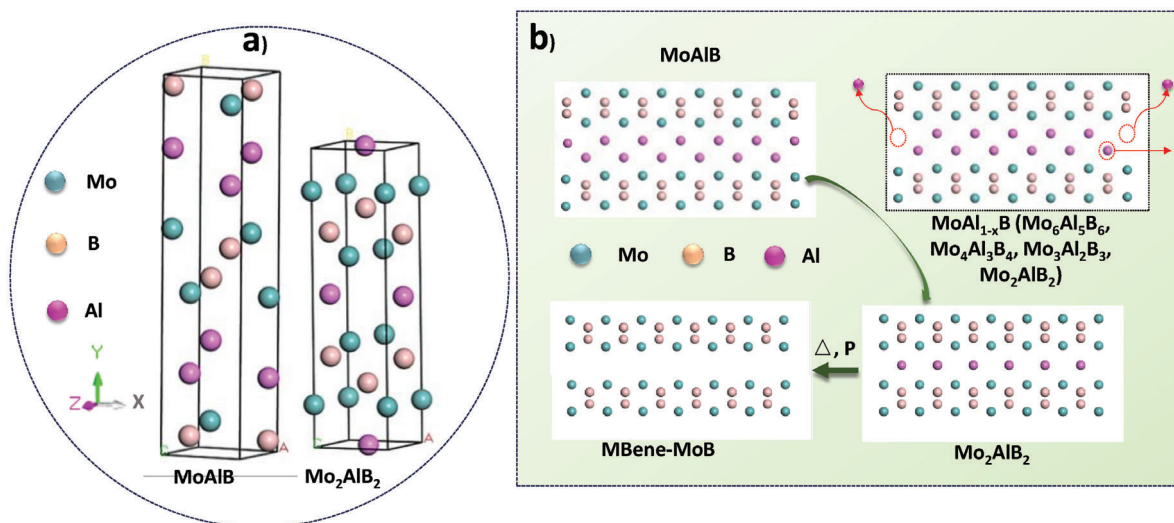NANO · MICRO
small
www.small-journal.com

Figure 1. a) Crystal structures of MoAlB and Mo_2AlB_2, b) schematic diagram of the aluminum removal process from MoAlB.

to discern the suitability of specific MBenes for distinct electrochemical applications. Notably, no singular MBene exhibits equal proficiency in both electrochemical catalysis and energy storage due to significantly different mechanisms.[11,15] Further research is imperative to investigate the suitability of a given MBene for both energy storage and electrocatalysis. Additionally, strategies must be proposed for modifying MBenes to enhance their performance in these predominantly distinct electrochemical applications.

This study delves into the controlled Al etching for layered $MoAl_{1-x}B$ formation from MoAlB, culminating in the achievement of complete aluminum dissipation MBene-MoB, highlighting its enhancing unique properties and applications. Through innovative etching processes in fluoride-free acidic/alkaline solutions, we achieved unprecedented results in terms of aluminum removal, yielding pristine single/few-layer MBene-MoB for the first time. The exploration of this synthesis pathway, coupled with a comprehensive understanding of the material's thermodynamics and kinetics, forms the crux of our investigation. In this context, we delve into the structural evolution of MBene-MoB through XRD refinement, tracking the removal of aluminum and identifying transient phases. The calculated electronic properties further underscore the exceptional conductivity of MBene-MoB and its precursor materials. Additionally, we elucidate the outstanding supercapacitor performance of MBene-MoB, outperforming many conventional 2D materials, and explore its potential catalytic prowess in hydrogen evolution reactions. This comprehensive investigation bridges the gap between MBenes synthesis, characterization, and practical applications, positioning MBene-MoB as a groundbreaking material in the landscape of advanced nanomaterials for energy storage and surface catalysis.

2. Results and Discussion

2.1. Preparation and Characterization

The crystal structure of MoAlB was refined by experimental XRD pattern, as illustrated in Figure S1 (Supporting Information), the

structure is shown in **Figure 1** and with detailed parameters presented in Table S2 (Supporting Information). The removal of an Al layer between adjacent Mo-B slabs facilitates the transformation of MoAlB into Mo_2AlB_2 (Figure 1). Upon complete removal of all Al, it converts into MoB layer MBene-MoB. The simulated structural parameters and XRD patterns are depicted in Figures S2 and S3 (Supporting Information), as well as summarized in Table S2 (Supporting Information). A significant volume change observed in Mo_2AlB_2 is primarily attributed to the reduction of the lattice constant "*b*," resulting in the formation of cracks perpendicular to the "*b*" direction (Figure 1). In dilute alkaline solutions, the Al-removal rate gradually increases with an elevated etching temperature (Table S3, Supporting Information). From the XRD results in **Figure 2**, it is evident that the conversion into Mo_2AlB_2 is not sudden, the (020) peak of MoAlB in the XRD pattern gradually shifts to a higher angle position. Before 50% Al removal, a broadened peak formed in the higher angle position, overlapping with the (020) peak of MoAlB. This phenomenon can be explained by the formation of a high density of stacking faults or the simultaneous formation of phases with different but smaller lattice constant "*b*." It is assumed that these multi-intergrowth phases ($Mo_6Al_5B_6$, $Mo_4Al_3B_4$, $Mo_3Al_2B_3$, and Mo_2AlB_2) have a similar crystal structure to that of MoAlB.[13a,16] Further removal of Al to ≈50%, as indicated in the fractions calculated from XRD data results (Table S3, Supporting Information), a complete conversion into stable Mo_2AlB_2 occurs. Subsequently, Mo_2AlB_2 acts as a precursor to few-layer or single-layer MBene-MoB. At 200 °C, pure MBene-MoB is obtained, characterized by the absence of obvious XRD peaks, signifying a loss of crystal form. The diagram in Figure 1b reveals the Aluminium removal process from MoAlB. Based on the formation energy chart depicted in Figure 2c, $MoAl_{0.5}B$ ($1/2$ Mo_2AlB_2) and MBene-MoB are derived from one unit of MoAlB by sequentially removing 0.5 Al and then 1 Al in total. This process results in formation energies of 0.424 and 1.401 eV above MoAlB, respectively. Notably, a B-Al covalent bond was identified in MoAlB. The presence of this covalent bonding in MoAlB renders the deintercalation of Al challenging, thereby impeding the selective etching out of Al for
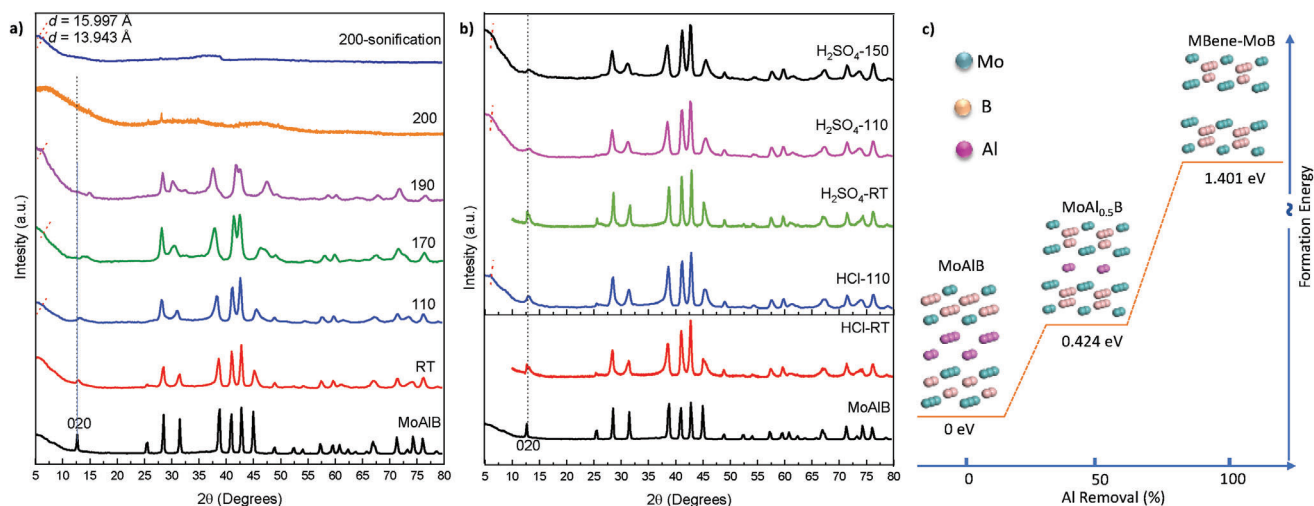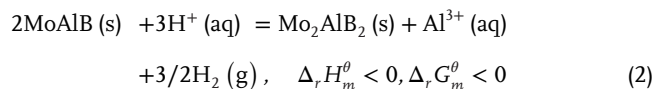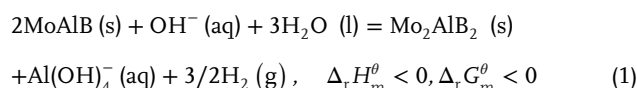
Figure 2. a) XRD patterns of MoAlB and its Al deficient products at different temperatures in 0.25 M NaOH, b) 0.25 M HCl and 0.25 M H_2SO_4 (RT and 110 is 0.25 M HCl or H_2SO_4, 150 is 0.5 M H_2SO_4), c) the formation energies of Mo_2AlB_2 (expressed in one unit of $MoAl_{0.5}B$) and MBene-MoB, using the energy of MoAlB as the baseline.

the preparation of 2D MoB. Once this covalent bond is overcome, the material transitions into a relatively stable intermediate state known as the intermediate transition state – Mo_2AlB_2. In this state, the B—Al bond is significantly weakened, acting as a precursor for MBenes.[13a,16] From this perspective, it is evident that both Mo_2AlB_2 and MBene exhibit lower stability compared to MoAlB, with MBene being the least stable, characterized by higher surface energy, is easily modulated by —O and —OH groups from the solution.

All the aluminium-defective samples exhibit significant d-spacing at lower X-ray diffraction (XRD) angles because of their layered structure. Additionally, from room temperature to 200 °C, thinner and thinner slabs are observed, as depicted in the scanning electron microscopy (SEM) images presented in **Figure 3**. After the intercalation of ammonium solution during sonication, the result is the formation of a few-layer or single-layer MBene-MoB. The ADF-STEM and BF-STEM images in Figure S4 (Supporting Information) provided additional confirmation of the layered structure observed in Mo_2AlB_2 and MBene-MoB. Additionally, TEM-EDS analysis corroborated the near-complete removal of Al in MBene-MoB. In Figure 3e of the High-Resolution TEM (HRTEM) image, a distinct lattice fringe spacing of the (020) planes with 0.707 nm of MoAlB is observed, upon the loss of 50% aluminum, the material transforms into a new phase, Mo_2AlB_2, with a reduced lattice spacing of 0.617 nm for the (020) crystal plane. This conclusion is further supported clearly by Selected Area Electron Diffraction (SAED) patterns. Subsequent complete loss of all Al leads to crystal structural collapse and reorganization, resulting in the formation of MoB, characterized by an amorphous, noncrystalline phase. While lattice fringes are not distinctly visible, partially restacked regions exhibiting a crystalline structure produce SAED patterns consistent with the (004) crystal planes of MoB (ICDD card No. 65–2753). These findings align with the X-ray diffraction (XRD) analysis.

In dilute acid, a certain degree of etching is achieved, resulting in multi-layered $MoAl_{1-x}B$, as shown in Figure 3 and

Table S3 (Supporting Information). Unfortunately, the etching rate stabilizes at ≈33%, and XRD results indicate that complete conversion into Mo_2AlB_2 does not occur in the acid, even with increased concentration and temperature. However, aluminum etching initiates at room temperature in both dilute acid and alkali solutions, prompting us to contemplate their distinct etching thermodynamics. The reactions can be deduced as follows, whether in an alkaline (Equation 1) or acid medium (Equation 2):

$$2MoAlB\ (s) + OH^-\ (aq) + 3H_2O\ (l) = Mo_2AlB_2\ (s)$$
$$+Al(OH)_4^-\ (aq) + 3/2H_2\ (g), \quad \Delta_r H_m^\theta < 0, \Delta_r G_m^\theta < 0 \quad (1)$$

$$2MoAlB\ (s)\ +3H^+\ (aq)\ = Mo_2AlB_2\ (s) + Al^{3+}\ (aq)$$
$$+3/2H_2\ (g), \quad \Delta_r H_m^\theta < 0, \Delta_r G_m^\theta < 0 \quad (2)$$

A thermodynamic analysis of these processes is provided in the Supporting Information. Thermodynamic analysis indicates that these are the two thermodynamically favorable reactions, as both enthalpy change and Gibbs free energy change are less than 0 (Supporting Information). This ease of etching is in contrast to MXene, which typically requires strong etchants or concentrated alkali at high temperatures. At room temperature, MoAlB etching is not complete in alkali, potentially due to the formation of some insoluble aluminum hydroxide, limiting further etching. The reaction between hydroxide ions (OH⁻) and aluminum hydroxides is inherently endothermic. Nevertheless, these insoluble impurities tend to dissolve further at higher temperatures, thereby prompting the equilibrium to shift in the forward direction, promoting additional aluminum etching. In acidic media, the dissolution of aluminum oxide/hydroxide layers is also thermodynamically favorable at room temperature. Therefore, the dynamic issue could be ascribed to the formation of pure Mo_2AlB_2 in acid etchants. Even at elevated temperatures or acid concentrations (0.5 M H_2SO_4), the reaction remains sluggish,

ADVANCED
SCIENCE NEWS
www.advancedsciencenews.com

NANO · MICRO
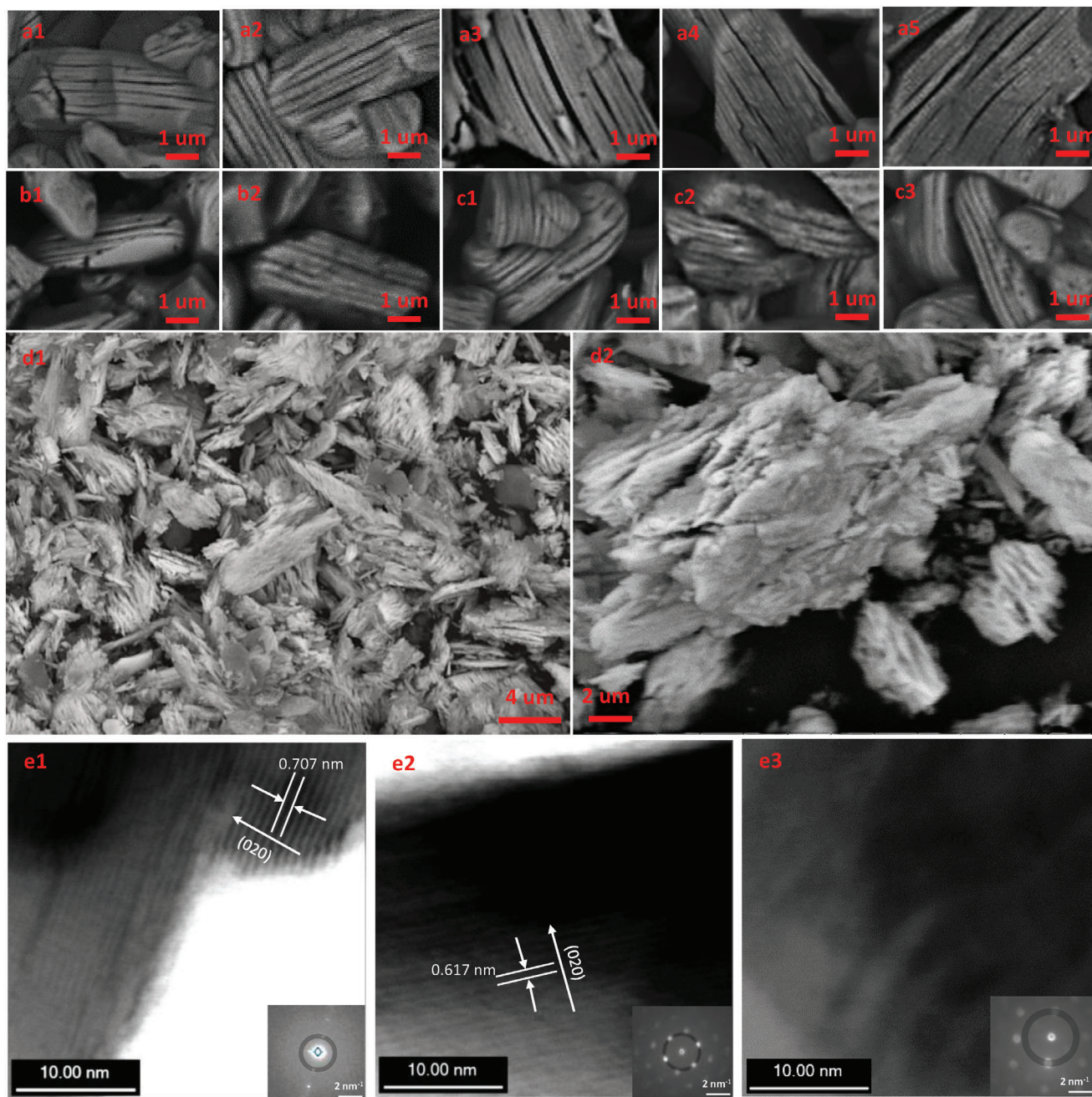small
www.small-journal.com

Figure 3. a) SEM photographs of MoAlB etched in 0.25 M NaOH at different temperatures for 6 h (a1–a5: RT, 110, 170, 190, 200 °C), b) in 0.25 HCl (b1–b2: RT and 110 °C, c) in H_2SO_4 (c1–c2: RT, 110 °C in 0.25 M, c3 is in 0.5 M 150 °C), d) MBene-MoB after sonification in ammonium aqueous for 1 h, e) HRTEM and inserted SAED images of MoAlB, Mo_2AlB_2 and MBene-MoB (from left to right).

necessitating further temperature increases. However, further raising the concentration of etching acid or temperature is economically impractical. Alkali, on the other hand, proves to be more suitable for etching, as it achieves 100% etching at 200 °C in even very dilute concentrations (0.25 M). From EDX analysis, no evidence of sulfate or chloride ions was observed after sulfuric acid or hydrochloric acid etching treatment, while FTIR testing in **Figure** 4a revealed surface products rich in —O and —OH functional groups both in acid and alkali etchants.

The X-ray photoelectron spectroscopy (XPS) spectra, depicted in Figure S4 (Supporting Information), along with high-resolution Al 2p spectra[17] in Figure 4c, unequivocally validate the thorough removal of aluminum. The fitted peak observed in the Mo 3d spectrum (Figure 4d) is attributed to $Mo^{4+}/Mo^{5+}/Mo^{6+}$ surface oxidation.[18] A binding energy (BE) of 230.7 eV (233.8 eV), is specifically assigned to HO/O—Mo—B in Table S4 (Supporting Information).[17] Notably, this BE is elevated by 2.7 eV compared to that for MoAlB, indicative of the removal

ADVANCED
SCIENCE NEWS

www.advancedsciencenews.com

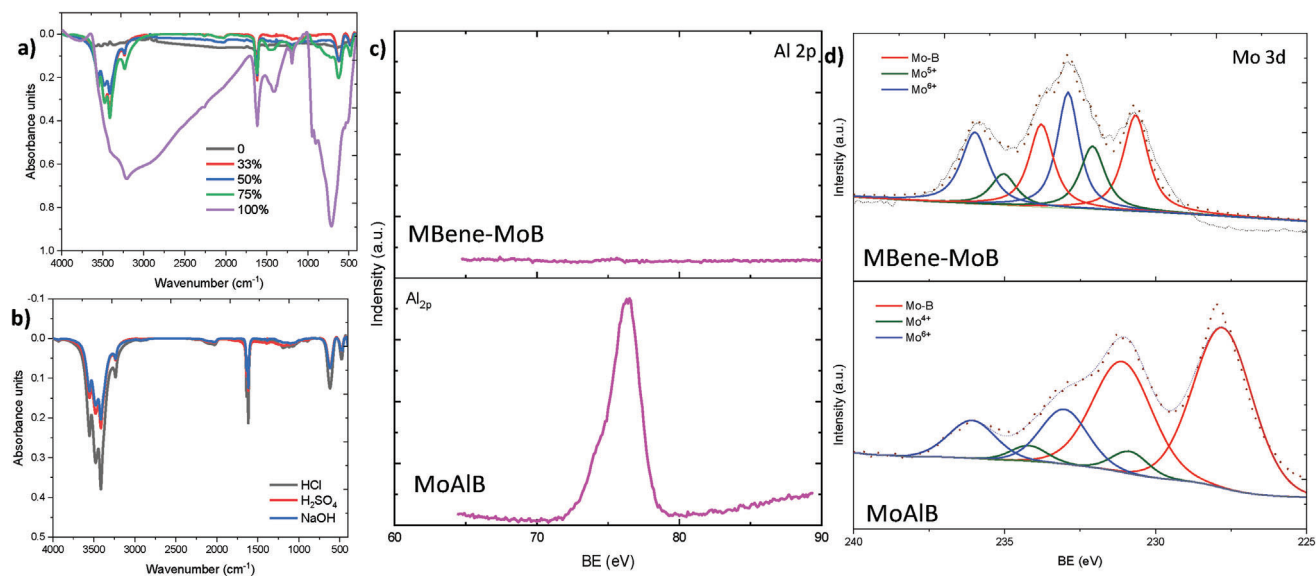NANO · MICRO

small

www.small-journal.com

Figure 4. a) FTIR spectra for pristine MoAlB and its different Al defective samples obtained from 0.25 NaOH etching, b) FTIR spectra of MoAlB with ≈33% Al defective in different etchants, high-resolution XPS spectra with peak fitting of c) Al 2p (*y-axis* have the same value scale) and d) Mo 3d for MoAlB (lower spectra) and MBene-MoB (upper spectra).

of aluminum and the incorporation of surface terminations in the form of —OH/—O groups. Furthermore, in Table S5 (Supporting Information), the increased fraction of B—O[19] becomes apparent post-Al removal, coinciding with the introduction of—O and —OH groups. These observations collectively corroborate the process of Al removal and underscore the elevation in the average chemical state of both molybdenum (Mo) and boron (B).

2.2. Electrochemical Properties

2.2.1. 3-Electrode System Supercapacitor

The graphical representation in **Figure 5a** illustrates the Galvanostatic Charge–Discharge (GCD) profiles of materials with varying aluminum stripping rates at a current density of 5 mA cm^{-2}. Additionally, Figures S5 and S6 (Supporting Information) provide detailed CV curves at different scan rates and GCD curves at different charge–discharge speeds, respectively. The corresponding specific capacitance values at 5 mA cm^{-2}, derived from the GCD profiles, are presented in Figure 5b. It is evident that as aluminum is progressively stripped, there is a gradual increase in specific capacitance, reaching a peak after complete aluminum loss. This enhancement can be attributed to the increasing specific surface area and the comprehensive exposure of active surfaces. A high capacitance of 4025.60 mF cm^{-2}/201.28 F g^{-1} surpasses that of many carbon or other 2D material electrodes, including MXenes, as shown in Table S6 (Supporting Information). Additionally, it exhibited a high Coulombic Efficiency of 92.27% at a low charge–discharge speed of 5 mA cm^{-2}. The cyclic voltammetry (CV) curves in Figure 5c reveal a deviation from rectangular shapes as aluminum is depleted, indicating a gradual rise in diffusion capacitance. This phenomenon significantly contributes to the observed increase in capacitance. As

depicted in Figure 5d, the material exhibits excellent cyclic performance even after 6000 cycles, maintaining a retention rate of 91.54%. This underscores the promising practical application prospects of MBene. Traditionally, the choice of etchants yields different terminal groups for MBenes or MXenes. However, in this study, etching with H$_2$SO$_4$ and HCl did not result in conspicuous —Cl and —SO$_4$ terminals, with primarily —OH and O$^-$ functionalities persisting. Interestingly, when subjected to acid or alkali etching and achieving equivalent aluminum removal rates, the capacitance performances (Figure 5e) exhibit minimal variations. This suggests that the predominant influencing factor is the extent of aluminum deintercalation. It is widely recognized that MoAlB (0.36–0.49 μΩ^{-1} m^{-1})[20] exhibits excellent conductivity, and the Total Density of States (TDOS) of Mo$_2$AlB$_2$ and MBene structures extends through the Fermi level (Figure 5f), indicating metallic properties remain after Al removal. Clearly, Al defective samples possess higher electron density near the Femi level, suggesting their enhanced electrical conductivity compared to the precursor MoAlB. MBene-MoB and MoAl$_{1-x}$B showed no dissolution during the electrotesting and electrode fabrication processes. Additionally, the XRD patterns of MoAl$_{0.2}$B did not exhibit significant changes before and after supercapacitor measurements in Figure S5i (Supporting Information), showcasing exceptional stability.

2.2.2. 2-Electrode Supercapacitor Device Set and ASSS

The supercapacitor performance and energy storage mechanism of MBene-MoB were further investigated in a 2-electrode device configuration. Two film-electrodes were prepared, sandwiching a cellular NKK separator in an aqueous symmetric two-electrode setup using Na$_2$SO$_4$ as the electrolyte. The charge storage capacity was primarily assessed through cyclic voltammetry (CV)

ADVANCED
SCIENCE NEWS

www.advancedsciencenews.com

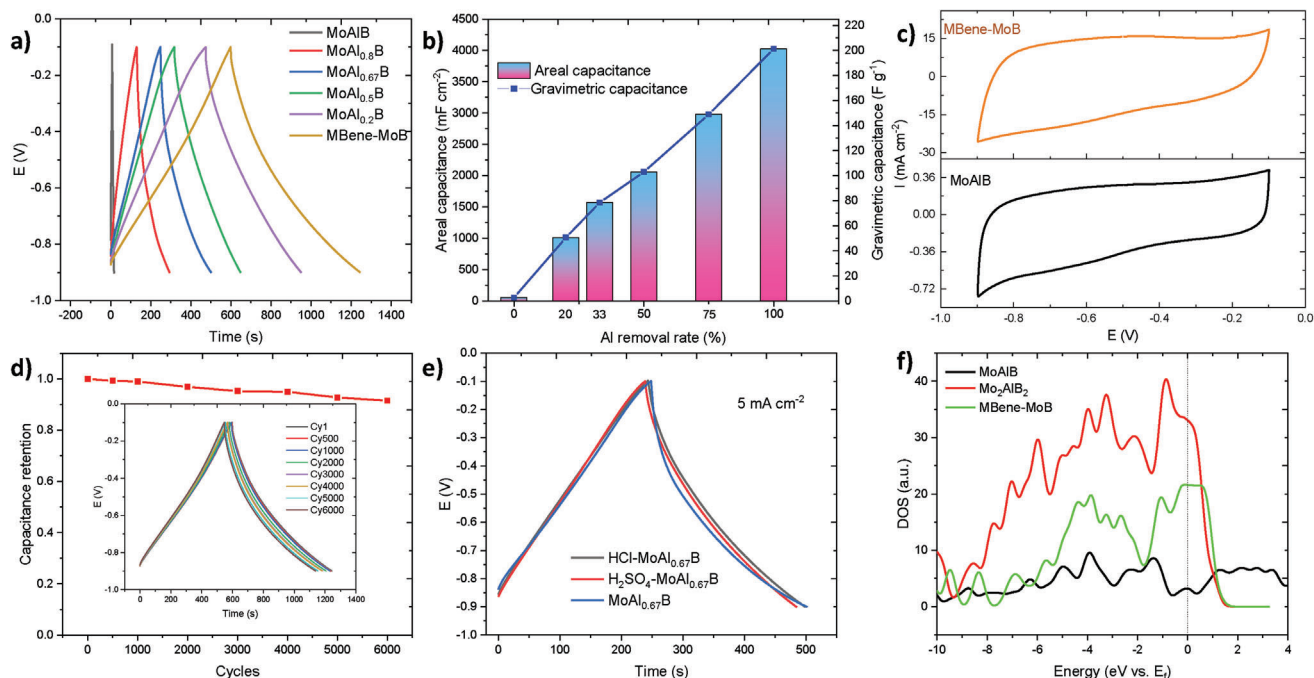NANO · MICRO

small

www.small-journal.com

Figure 5. Electrochemical measurements in 3-electrode set: a) GCD curves for different electrodes at the different charge–discharging speed of 5 mA cm^{-2} in 1 M Na$_2$SO$_4$, b) areal and gravimetric capacitance results calculated from GCD curves (5 mA cm^{-2}), c) CV curves for MoAlB and MBene-MoB at 5 mV s^{-1} scan rate, respectively, d) capacitance retention of MBene-MoB electrode at 5 mA cm^{-2} charge–discharge speed (inset is GCD curve in different number of GCD cycles), e) GCD curves for MoAl$_{0.67}$B, HCl-MoAl$_{0.67}$B and H$_2$SO$_4$-MoAl$_{0.67}$B, respectively, f) total density of state (TDOS) of MoAlB, Mo$_2$AlB$_2$ and MBene-MoB, respectively.

measurements at various scan rates within a potential window of 0–1 V (**Figure** 6a). The observed increase in current with higher scan rates indicated favorable performance. In this supercapacitor device, a high areal capacitance of 1816.85 mF cm^{-2} (5 mA cm^{-2}) for the entire device calculated from Figure 6b GCD curves and 3633.7 mF cm^{-2} for a single electrode were achieved (Figure 6c), Additionally, the material demonstrated a relatively high capacitance performance of 589.41 mF cm^{-2} at a high charge–discharge rate of 30 mA cm^{-2}. The outstanding performance can be attributed to efficient ion-diffusion and ultra-low resistance, as illustrated in Figure 6d. The intercept on the horizontal axis and the semicircular arc at high frequency represent the solution resistance (R$_S$) and charge transfer resistance (R$_{ct}$), respectively. These values, calculated from equivalent circuit fitting (inset of Figure 6d), were found to be 0.0448 Ω cm^{-2} and 0.00347 Ω cm^{-2}, significantly lower than those of MXene-based electrodes.[3a,21] To further validate the impedance behavior, a complex model of capacitance was employed (Equations S7 and S8, Supporting Information). The relaxation time constant (τ_0), calculated from the peak position for imaginary capacitance C″(ω), was notably short at τ_0 = 3.25 s (Figure 6e), indicating high charge transport kinetics. These results confirm the superior performance of MBene-MoB, showcasing its potential for advanced applications in energy storage.

Generally, capacitance can be classified into surface-controlled capacitance and diffusion-controlled pseudo-capacitance.[22] Electrochemical kinetics analysis was conducted using the CV method with Equations S9 and S10 (Supporting Information). The b-value, obtained from the log(i) versus log(v) plot, serves as an indicator of the underlying capacitance process. In an ideal surface capacitance process, the b-value is 1, while for a sole pseudo-capacitance process, it is 0.5. A b-value ranging between 0.5 and 1 indicates the coexistence of both capacitance processes.[9] In Figure S7a (Supporting Information), the observed b-values ranging from 0.5 to 1 indicate the simultaneous presence of surface-controlled and diffusion-controlled capacitance during charge–discharge. To further quantify the surface-controlled contribution to the overall current response, Dunn's method (Equations S11 and S12 Supporting Information) were employed: current divided by the square root of the scan rate response to the square root of the scan rate, shown in Figure S7b (Supporting Information). The distribution shifted with an increase in the scan rate, with the surface-controlled contribution escalating from 33.8% to 88.7%, and the diffusion-controlled contribution declining from 66.2% to 11.3% (Figure 6f). The prominent interlayer structure contributes to surface capacitance, while the ultra-high conductivity facilitates high diffusion-controlled pseudo-capacitance. This hybrid charge storage mechanism proves advantageous for enhancing both energy and high-power densities, all the while maintaining excellent stability. Table S7 (Supporting Information) and Ragone plot in Figure 6g illustrates the device's areal energy density ranging from 252.34 to 81.86 μWh cm^{-2}, corresponding to power densities of 2.5–15 mW cm^{-2}. This performance surpasses many previously reported supercapacitors ensembles, including those based on metal oxide,[23] MXenes-based,[23c,24] molybdenum-based,[9] carbon-based,[23b,24b,25] and conductive polymers.[22,25b] In a two-electrode system, Coulombic efficiency

ADVANCED
SCIENCE NEWS
www.advancedsciencenews.com
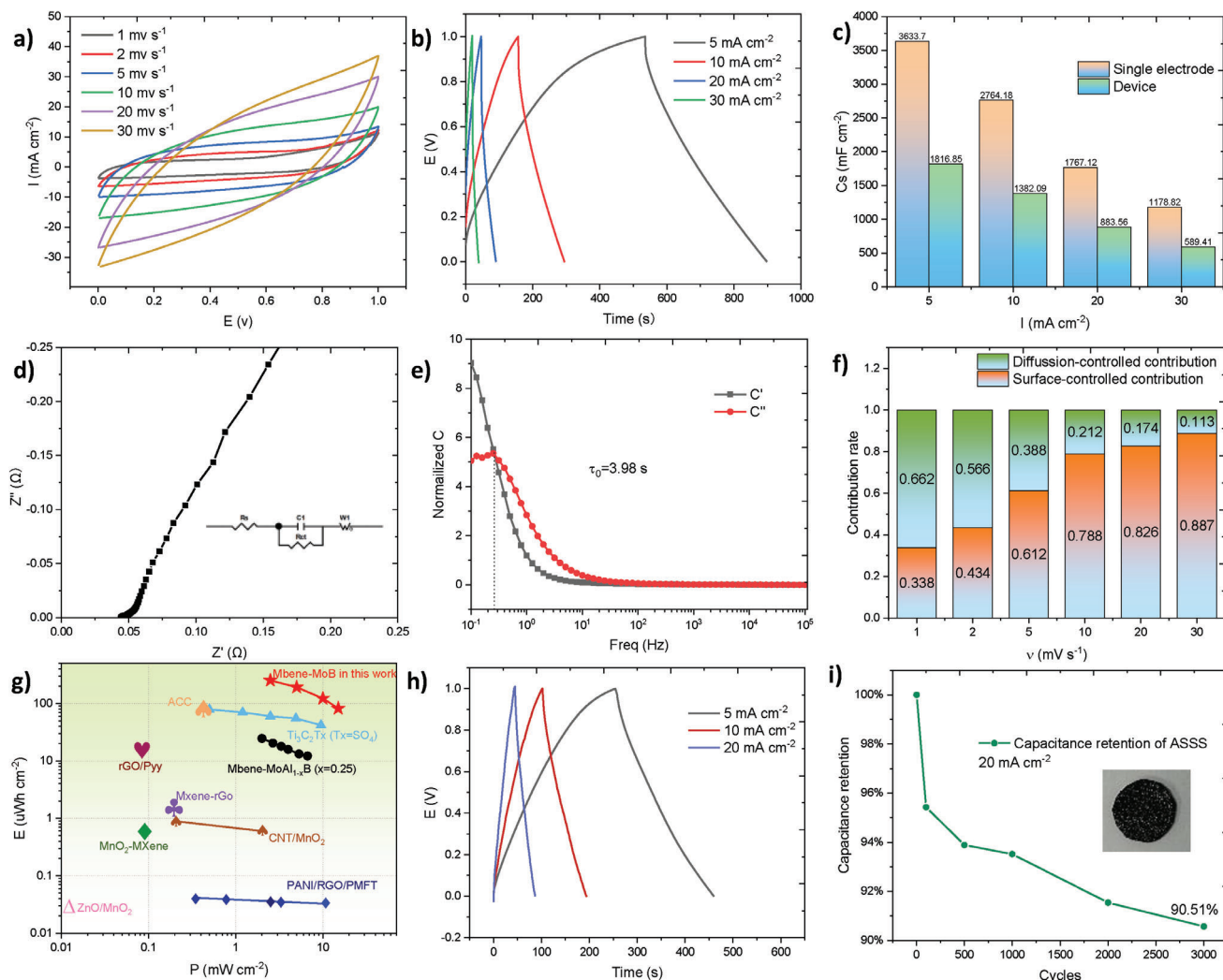
NANO · MICRO
small
www.small-journal.com

Figure 6. Electrochemical measurements for MBene-MoB in 2-electrode device set: a) CV curves at different scan rates, b) GCD curves at different charge–discharging speeds, c) areal capacitance C_S (mF cm^{-2}) for whole device and single electrode, d)Nyquist plots obtained by electrochemical impedance spectroscopy EIS with enlargement and equivalent series resistance (ESR) in the insets, e) evolution of imaginary and real part of the capacitance versus frequency, f) the proportions of the surface-controlled and confusion-controlled capacitive contribution at different scan rates, g) Ragone plot showing energy density versus power density, h) GCD curves of ASSS, i) capacitance retention of ASSS at 20 mA cm^{-2} (insert is the picture of ASSS).

gradually improves with the charge–discharge rate. At a current density of 30 mA cm^{-2}, the Coulombic efficiency reaches 98.84%. However, due to the working voltage window being 1 V, Coulombic efficiency isn't optimal at low charge–discharge rates, mainly due to the necessity to overcome water splitting and electrolyte-electrode contact resistance, resulting in a certain voltage drop (IR drop). Therefore, to further assess the material's practical application, it was encapsulated into an all-solid-state supercapacitor (ASSS). As depicted in Figure 6h and Table S8 (Supporting Information), even at low charge–discharge rates of 5 mA cm^{-2}, the Coulombic efficiency of ASSS is at a high level and its capacitive performance is excellent, reaching 1066.39 mF cm^{-2} @ 5 mA cm^{-2} for the device. Moreover, under high charge–discharge rate conditions, cyclic performance remains robust. After 3000 cycles of charge–discharge operation, as observed in Figure 6i, the capacitance retention

rate also exceeds 90%, highlighting its practical application potential.

The diffusion of electrolyte ions is a crucial aspect during the charge–discharge process in diffusion-controlled capacitors. To gain a deeper understanding of the migration process of electrolyte ions on the MBene-MoB surface, the adsorption energy of Na$^+$ on the 2D MoB surface was calculated using density functional theory (DFT). In **Figure 7a**, three distinct adsorption sites were chosen: above the B atom (−2.737 eV), above the Mo atom (−2.591 eV), and in the hollow of 2 Mo and 2 B atoms (−2.619 eV). Notably, the highest adsorption energy is observed when the Na ion is adsorbed above the B atom. To elucidate the Na ion diffusion characteristics, the Complete LST/QST method in CASTEP was employed. In Figure 7b, P1 and P2 represent the starting and ending points of the migration process, and the calculated diffusion energy barrier along this path was found to be 0.144 eV. The
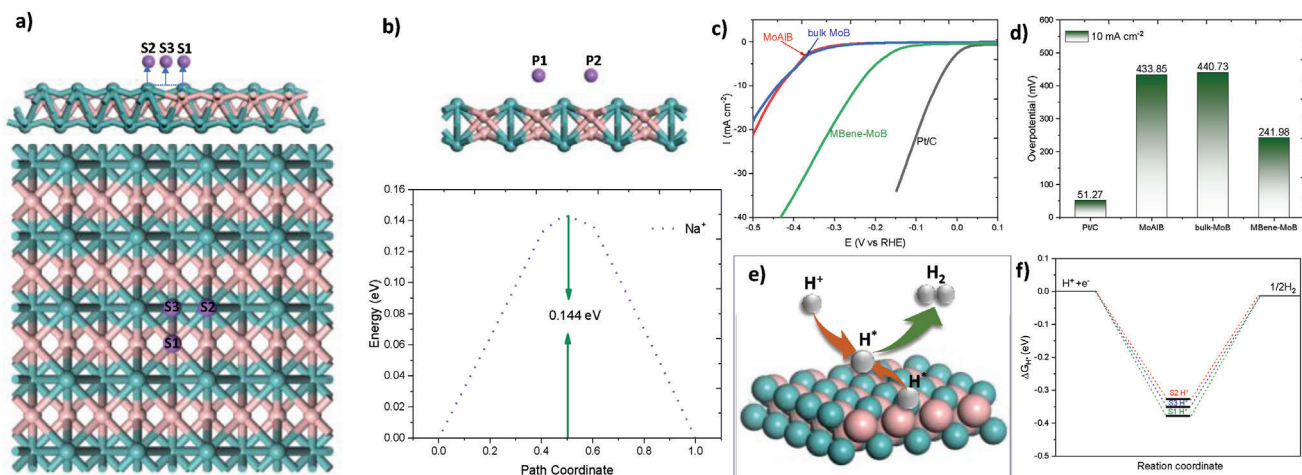
**ADVANCED
SCIENCE NEWS**

www.advancedsciencenews.com

**NANO · MICRO
small**

www.small-journal.com

Figure 7. a) Na$^+$ adsorbed on MBene-MoB, b) migration barrier map of Na ion on the MBene surface, c,d) HER electrocatalysis data for MBene-MoB, MoAlB, commercial-MoB with similar particle size, and Pt/C in 0.5 M H$_2$SO$_4$, e) HER mechanisms in acidic medium, f) adsorption energy of H* on the different sites of MBene-MoB surface.

ion diffusion plays a pivotal role in influencing the charge and discharge speed as well as the cyclic performance of capacitors. A lower diffusion barrier significantly enhances the frequency response. These results substantiate that Na ions in the electrolyte exhibit rapid diffusion on the MoB surface.

2.2.3. HER Properties

The Linear Sweep Voltammetry data for MoAlB, bulk-MoB, and MBene-MoB, all exhibiting similar grain sizes, are presented in Figure 7c,d for the Hydrogen Evolution Reaction (HER) in a 0.5 M H$_2$SO$_4$ solution. Remarkably, MBene-MoB demonstrates significantly superior catalytic activity compared to both bulk MoB and the precursor MoAlB, despite similar grain sizes. These findings affirm the catalytic potential of layered MBene-MoB and underscore the accessibility of its interlamination. The observed enhancement in HER activity of MoAlB after etching can be attributed to the increased surface area of catalytically active basal planes exposed through the selective leaching of aluminum from the layered crystal structure. The recorded overpotential of 241.98 mV at 10 mA cm^{-2} on a reversible hydrogen electrode for MBene-MoB indicates moderate activity, positioning it favorably relative to some of the most efficient nonprecious metal HER catalysts. While there is room for improvement in MBene's hydrogen catalysis, its evident potential remains promising.

In acidic environments, the Hydrogen Evolution Reaction (HER) manifests through two distinct mechanisms, as depicted in the accompanying Figure 7e. First, hydrogen ions in the solution approach the surface of the adsorbent, gaining an electron to form adsorbed hydrogen atoms. One pathway involves the reaction of hydrogen ions in the solution with these adsorbed hydrogen atoms, resulting in the generation of a hydrogen molecule (Volmer–Heyrovsky mechanism). Alternatively, when the adsorption of hydrogen atoms on the catalyst surface is prevalent, two hydrogen atoms come together to generate a hydrogen molecule (Volmer–Tafel mechanism). In this process, the

adsorption energy of hydrogen atoms is crucial, ideally approaching zero. Computational analysis reveals that MBene-MoB exhibits relatively higher adsorption energy for H* (Figure 7f, adsorption calculated at three positions consistent with the abovementioned Na$^+$ adsorption), potentially impeding the facile release of hydrogen gas after its generation. Despite this, the performance falls within the moderate range among non-noble metals, and MBene demonstrates outstanding conductivity. Future research avenues may explore strategies such as doping or other surface modifications to further reduce this adsorption energy, facilitating the efficient release of hydrogen gas postgeneration. This targeted approach aims to enhance the overall performance of the Hydrogen Evolution Reaction for MBenes.

3. Conclusion

In conclusion, the thermodynamically favorable process of aluminum etching from MoAlB, conducted in fluoride-free dilute acidic/alkaline solutions at room temperature (RT), initiates the removal of aluminum. Subsequently, the synthesis yields pure single/few-layered MBene-MoB, achieved at 200 °C in a hydrothermal environment with a 0.25 M NaOH solution. The structural evolution, delineated through XRD refinement, meticulously traces the transition from transient unstable phases MoAl$_{1-x}$B (x < 0.5) to a relatively stable Mo$_2$AlB$_2$ structure, establishing a clear precursor-product relationship. Significantly, the calculated electronic properties affirm the exceptional conductivity of MBene-MoB and its precursor material. As Al is gradually removed, the capacitance increases, and the supercapacitor performance of MBene-MoB surpasses that of conventional 2D materials. This success can be attributed to a synergistic combination of surface-controlled and diffusion-controlled capacitance storage mechanisms, and rapid electrolyte diffusion within the interlamellar. In the context of hydrogen evolution reactions (HER), MBene-MoB exhibits a moderate overpotential of 241.98 mV at 10 mA cm^{-2} due to its high hydrogen adsorption energy. Nevertheless, the material's exceptional conductivity,

**ADVANCED
SCIENCE NEWS**

www.advancedsciencenews.com

NANO · MICRO
small

www.small-journal.com

coupled with rapid electrolyte diffusion, positions MBene-MoB as a compelling candidate for HER applications. In essence, MBene-MoB serves as a paradigm of excellence in transition metal boride nanomaterials, offering a unique combination of synthesis simplicity, structural stability, and versatile electrochemical performance.

Supporting Information

Supporting Information is available from the Wiley Online Library or from the author.

Conflict of Interest

The authors declare no conflict of interest.

Author Contributions

S.W. performed methodology, software, experiments, simulation, formal analysis, and data curation, wrote—original draft. G.M.K. performed formal analysis, methodology, review, and supervision. X.L. performed review and supervision.

Data Availability Statement

The data that support the findings of this study are available in the supplementary material of this article.

[1] a) M. S. Javed, A. Mateen, I. Hussain, S. Ali, S. Asim, A. Ahmad, E. tag Eldin, M. A. Bajaber, T. Najam, W. Han, *Chem. Eng. J.* **2023**, *452*, 139455; b) H. Tao, Q. Fan, T. Ma, S. Liu, H. Gysling, J. Texter, F. Guo, Z. Sun, *Prog. Mater. Sci.* **2020**, *111*, 100637; c) A. Sharma, V. S. Rangra, A. Thakur, *Prog. Mater. Sci.* **2022**, *57*, 12738.

[2] a) Q. Jiang, Y. J. Lei, H. F. Liang, K. Xi, C. Xia, H. N. Alshareef, *Energy Storage Mater.* **2020**, *27*, 78; b) K. N. Dinh, Q. H. Liang, C. F. Du, J. Zhao, A. L. Y. Tok, H. Mao, Q. Y. Yan, *Nano Today* **2019**, *25*, 99.

[3] a) M. Guo, C. B. Liu, Z. Z. Zhang, J. Zhou, Y. H. Tang, S. L. Luo, *Adv. Funct. Mater.* **2018**, *28*, 1803196; b) T. Li, L. Yao, Q. Liu, J. Gu, R. Luo, J. Li, X. Yan, W. Wang, P. Liu, B. Chen, W. Zhang, W. Abbas, R. Naz, D. Zhang, *Angew. Chem., Int. Ed.* **2018**, *57*, 6115; c) D. Jiang, C. J. O. Bacal, K. A. S. Usman, J. Zhang, S. Qin, D. Hegh, W. Lei, J. Liu, J. M. Razal, *Adv. Mater. Technol.* **2023**, *8*, 2201611.

[4] F. Cao, Y. Zhang, H. Wang, K. Khan, A. K. Tareen, W. Qian, H. Zhang, H. Ågren, *Adv. Mater.* **2022**, *34*, 2107554.

[5] a) X. W. Yang, C. J. Shang, S. Zhou, J. J. Zhao, *Nanoscale Horiz.* **2020**, *5*, 1106; b) N. F. Rosli, M. Z. M. Nasir, N. Antonatos, Z. Sofer, A. Dash, J. Gonzalez-Julian, A. C. Fisher, R. D. Webster, M. Pumera, *ACS Appl. Nano Mater.* **2019**, *2*, 6010.

[6] J. R. He, A. Bhargav, A. Manthiram, *Adv. Mater.* **2020**, *32*, 2004741.

[7] N. Miao, Y. Gong, H. Zhang, Q. Shen, R. Yang, J. Zhou, H. Hosono, J. Wang, *Angew. Chem., Int. Ed.* **2023**, *62*, 202308436.

[8] K. Liu, B. Zhang, X. Chen, Y. Huang, P. Zhang, D. Zhou, H. Du, B. Xiao, *J. Phy. Chem. C* **2021**, *125*, 18098.

[9] S. Wei, X. Lai, G. M. Kale, *ACS Appl Mater. Inter.* **2023**, *15*, 33560.

[10] L. T. Alameda, C. F. Holder, J. L. Fenton, R. E. Schaak, *Chem. Mater.* **2017**, *29*, 8953.

[11] Y. Zhang, Y. Zhang, Z. Guo, Y. Fang, C. Tang, N. Miao, B. Sa, J. Zhou, Z. Sun, *J. Colloid Interf. Sci.* **2023**, *652*, 1954.

[12] M. Khazaei, J. Wang, M. Estili, A. Ranjbar, S. Suehara, M. Arai, K. Esfarjani, S. Yunoki, *Nanoscale* **2019**, *11*, 11305.

[13] a) L. T. Alameda, P. Moradifar, Z. P. Metzger, N. Alem, R. E. Schaak, *J. Am. Chem. Soc.* **2018**, *140*, 8833; b) K. Kim, C. Chen, D. Nishio-Hamane, M. Okubo, A. Yamada, *Chem. Commun.* **2019**, *55*, 9295.

[14] a) K. J. Baumler, O. S. Adams, R. E. Schaak, *Chem. Commun.* **2023**, *59*, 4814; b) J. Mou, S. Li, W. Zhang, W. Xu, S. Fan, G. Bei, *J. Adv. Ceram.* **2023**, *12*, 943.

[15] Z. L. Guo, J. Zhou, Z. M. Sun, *J. Mater. Chem. A* **2017**, *5*, 23530.

[16] Y. Zhou, H. Xiang, H. Zhang, F.-Z. Dai, *J. Mater. Sci. Technol.* **2019**, *35*, 2926.

[17] V. Natu, S. S. Kota, M. W. Barsoum, *J. Eur. Ceram. Soc.* **2020**, *40*, 305.

[18] R. Escamilla, E. Carvajal, M. Cruz-Irisson, F. Morales, L. Huerta, E. Verdin, *J. Mater. Sci.* **2016**, *51*, 6411.

[19] A. R. Burke, C. R. Brown, W. C. Bowling, J. E. Glaub, D. Kapsch, C. M. Love, R. B. Whitaker, W. E. Moddeman, *Surf. Interface Anal.* **1988**, *11*, 353.

[20] S. Kota, E. Zapata-Solvas, A. Ly, J. Lu, O. Elkassabany, A. Huon, W. E. Lee, L. Hultman, S. J. May, M. W. Barsoum, *Sci. Rep.* **2016**, *6*, 26475.

[21] a) M. S. Javed, X. F. Zhang, S. Ali, A. Mateen, M. Idrees, M. Sajjad, S. Batool, A. Ahmad, M. Imran, T. Najam, W. H. Han, *Nano Energy* **2022**, *101*, 107624; b) J. Wang, D. Jiang, Y. Du, M. Zhang, Y. Sun, M. Jiang, J. Xu, J. Liu, *Small* **2023**, *19*, 2303043.

[22] X. L. Li, L. B. Yuan, R. Liu, H. N. He, J. N. Hao, Y. Lu, Y. M. Wang, G. M. Liang, G. H. Yuan, Z. P. Guo, *Adv. Energy Mater.* **2021**, *11*, 2003010.

[23] a) J. Bae, M. K. Song, Y. J. Park, J. M. Kim, M. Liu, Z. L. Wang, *Angew. Chem., Int. Ed.* **2011**, *50*, 1683; b) P. Xu, B. Wei, Z. Cao, J. Zheng, K. Gong, F. Li, J. Yu, Q. Li, W. Lu, J.-H. Byun, B.-S. Kim, Y. Yan, T.-W. Chou, *ACS Nano* **2015**, *9*, 6088; c) H. Jiang, Z. Wang, Q. Yang, M. Hanif, Z. Wang, L. Dong, M. Dong, *Electrochim. Acta* **2018**, *290*, 695.

[24] a) M. Guo, W. C. Geng, C. B. Liu, J. Y. Gu, Z. Z. Zhang, Y. H. Tang, *Chem. Mater.* **2020**, *32*, 8257; b) Y. Yue, N. Liu, Y. Ma, S. Wang, W. Liu, C. Luo, H. Zhang, F. Cheng, J. Rao, X. Hu, J. Su, Y. Gao, *ACS Nano* **2018**, *12*, 4224.

[25] a) Y.-J. Gu, W. Wen, J.-M. Wu, *J. Mater. Chem. A* **2018**, *6*, 21078; b) J. Cao, Y. Wang, J. Chen, X. Li, F. C. Walsh, J.-H. Ouyang, D. Jia, Y. Zhou, *J. Mater. Chem. A* **2015**, *3*, 14445.